



1
2
3
4
5
6
7
8
9
10
11
12
13
14
15
16
17
18
19
20
21
22
23
24
25
26
27
28
29
30
31
32
33
34
35
36
37
38
39
40
41
42
43
44
45
46
47
48
49
50
51
52

**Modeling a tropical-like cyclone in the Mediterranean Sea
under present and warmer climate**

Shunya Koseki¹, Priscilla A. Mooney², William Cabos³,
Miguel Ángel Gaertner⁴, Alba de la Vara⁴, Juan Jesus González Alemán⁵

- 1: Geophysical Institute, University of Bergen / Bjerknes Centre for Climate Research, Bergen, NORWAY*
2: NORCE Norwegian Research Centre AS / Bjerknes Centre for Climate Research, Bergen, NORWAY
3: Departamento de Ciencias Física, Universidad de Alcalá, Alcalá de Henares, SPAIN
4: Facultad de Ciencias del Medio Ambiente, Universidad de Castilla-La Mancha, Toledo, SPAIN
5: Departamento de Física de la Tierra y Astrofísica, Universidad Complutense de Madrid, Madrid, SPAIN

Correspondence to Shunya Koseki
Address: Allégate 70, 5007, Bergen, Norway
Email: Shunya.Koseki@gfi.uib.no



53 **Abstract**

54 This study focuses on a single Mediterranean hurricane (hereafter medicane), to investigate the
55 medicane response to global warming during the middle of the 21st century and assess the
56 contradictory effects of a warmer ocean and a warmer atmosphere on its development. Our
57 investigation uses the state-of-the-art regional climate model WRF with the optimum combination
58 of physical parameterizations based on a sensitivity assessment study. Results show that our model
59 setup can reproduce a realistic cyclone track and the transition from initial disturbance to tropical-
60 like cyclone with a deep warm core although the transition is earlier than for the observed
61 medicane. To investigate the response of the medicane to future climate change, a pseudo global
62 warming (PGW) approach has been used. This approach adds the projected change of atmospheric
63 and ocean variables obtained by an ensemble of CMIP5 models to the boundary conditions for the
64 regional climate model. A PGW simulation where all variables (PGW_{ALL}) are incremented shows
65 that most of the medicane characteristics moderately intensify, e.g., surface wind speed, uptake of
66 water vapour and precipitation. However the maximum depression of sea level pressure (SLP) is
67 almost identical with that under present climate conditions. Two additional PGW simulations were
68 undertaken; One simulation adds the projected change in sea surface and skin temperature only
69 (PGW_{SST}) while the second simulation adds the PGW changes to only atmospheric variables
70 (PGW_{ATMS}) i.e. we use present time sea surface temperatures. These simulations show opposite
71 effects on the medicane. In PGW_{SST}, the medicane is reinforced more vigorously than PGW_{ALL}:
72 much deeper SLP depression, stronger surface wind, and more intense evaporation and
73 precipitation. In contrast, the medicane in PGW_{ATMS} weakens considerably (SLP, surface wind and
74 rainfall decrease) still converts into a tropical-like cyclone with a deep warm core. This difference
75 can be explained by an increased water vapour driven by the warmer ocean surface (favourable for
76 cumulus convection) and the warmer and drier atmosphere in PGW_{ATMS} tends to inhibit
77 condensation (unfavourable for cumulus convection). As a result of these counteracting effects of
78 warmer ocean and atmosphere, the medicane is enhanced only modestly by global warming.

79
80
81
82
83
84
85
86
87



88 **1. Introduction**

89 It is well known that severe cyclonic storms occur in the Mediterranean Sea, in particular,
90 from September to March (e.g., Cavicchia et al., 2013). These cyclonic storms occasionally develop
91 into meso-scale cyclones with a cloud-free “eye” around the cyclone centre, which is also a
92 common typical feature of tropical cyclones. They generate vigorous precipitation and intense
93 wind, resulting in disastrous damages on regional economies and infrastructure over the coastal
94 areas in the Mediterranean nations (e.g., Bakkensen, 2017). These tropical-like cyclones are called
95 Mediterranean hurricanes or medicanes even though their lifetime as tropical-like cyclones is
96 shorter than most tropical cyclones. In general, the initiation and development of a tropical cyclone
97 requires certain physical and dynamical conditions (e.g., Camargo et al., 2007). One of these is
98 warm sea surface temperature (SST) like the warm pool in the tropical western Pacific Ocean.
99 However, the autumn and winter SST in the Mediterranean Sea varies from around 18°C to, at
100 highest, 23°C in the current climate (e.g., Shaltout and Omstedt, 2014; Fig. 2a), which is much
101 lower than tropical SST and the generation of tropical cyclone is quite rare over such cold SST (cf.
102 Pacific and Atlantic cold tongue, e.g., Jin 1996; Caniaux et al., 2011) even in the tropics.

103 The mechanism of medicane development has been investigated in previous studies. Similar
104 to tropical cyclones, an initial atmospheric disturbance is essential for medicane genesis. In many
105 cases, medicanes arise from cut-off lows isolated from the extratropical jet stream in the upper
106 troposphere (e.g., Emanuel, 2005; Fita et al., 2006; Chaboureaud, et al., 2012). Such a cut-off low
107 and a potential vorticity anomaly are pre-conditional for medicane initiation. This triggers deep
108 cumulus convection resulting in the formation of a deep warm core and consequently, a tropical
109 transition of the initial perturbation occurs (Mazza et al., 2017; Fita and Flaouanas, 2018). Miglietta
110 and Rotunno (2019) showed the importance of air-sea interactions for the development of two
111 medicanes. These discrepancies in the literature may arise from the dependency of the various
112 studies on individual case studies. The surface wind associated with the cyclonic circulation induces
113 the turbulent heat fluxes effectively and cumulus convection and diabatic heating are enhanced
114 (wind-induced surface heat exchange, WISHE, e.g., Emanuel, 1986).

115 In both mechanisms of medicane development and tropical transition, diabatic heating due
116 to condensation plays a vital role. As such understanding the response of medicane features to
117 anthropogenic global climate change is important for mitigating future risks associated with these
118 natural hazards. According to Shaltout and Omstedt (2014), the Mediterranean SST is expected to
119 increase by 2.6°C per century. This warming in the ocean can be a potential source of enhanced
120 moisture to the atmosphere. In fact, significant changes in medicanes e.g., frequency and intensity
121 associated with global warming have been reported in previous studies. Cavicchia (2014) showed
122 that whereas the frequency of medicanes tends to decrease, medicanes can moderately intensify



123 based on a climate projection with a global coupled model. Tous et al. (2016) also suggested similar
124 future changes in frequency and intensity of medicanes. Their study also revealed that the location
125 of medicane formation is expected change (more frequent over the Gulf of Lion-Genova and South
126 of Sicily). González-Alemán et al. (2019) concluded that associated with medicanes intensification,
127 the structure of tropical-like cyclones is more robust and their life-time as tropical-like cyclones is
128 longer-lasting compared to medicanes under current climate. This, consequently, leads to more
129 hazardous situations in the projected future.

130 Most of the aforementioned studies on the future climate of medicanes are based on results
131 obtained from global coupled models (CGCMs). However, in long climatic simulations performed
132 with CGCMs, the typical grid spacing varies between 100km and 25km at best. Even simulations at
133 25km are still insufficient to resolve the fine-scale structure of medicanes such as the cyclone core
134 and associated rain bands; the intensity of medicanes is underestimated in several coupled regional
135 models (Gaertner et al. 2018). Therefore, it is most likely that CGCMs also underestimate future
136 changes in medicanes. One possible solution to this problem is to dynamically downscale the global
137 models with a regional climate model (RCM) at finer resolutions. Alternatively, a pseudo global
138 warming method (PGW, e.g., Schär et al., 1996; Rasmussen et al., 2011; Parker et al., 2018;
139 Mooney et al., in review) can be used to assess more explicitly the impacts of future climate change
140 on medicanes. PGW is an advantageous method to characterize a given medicane in current and
141 future climate by imposing the future changes in atmospheric and ocean variables estimated by
142 CGCMs to boundary conditions of a high-resolution RCM (see details in Section 2). This approach
143 permits a more direct assessment of impacts of future climate change on an extreme weather event
144 (e.g., Parker et al., 2018). Additionally, the PGW method enables investigations of the relative roles
145 of a warmer atmosphere and a warmer ocean in the response of medicanes to climate change.

146 In this study, based on a PGW framework, we investigate the impacts of global warming on
147 the development and intensity of medicane Rolf (Miglietta et al., 2013; Ricchi et al., 2017; Dafis et
148 al., 2018). Rolf occurred from 6th to 9th November in 2011 and affected the Balearic Islands, Italy
149 and south France due to longer persistence of tropical-cyclonic features. Rolf is the first tropical
150 cyclone officially monitored by the National Oceanic and Atmospheric Administration (NOAA).
151 Since Rolf was a highly destructive medicane for coastal communities in many Mediterranean
152 countries, it is important to assess how these types of medicanes will respond to climate change in
153 near future. We perform additional idealised experiments in which only the atmosphere or the
154 ocean, respectively, experience global warming to elucidate the roles of a warmer atmosphere and a
155 warmer ocean on the medicane. This study is structured as follows. In Section 2, details of the
156 reanalysis data, RCM and experimental designs are provided. An evaluation and assessment of the
157 simulation of medicane Rolf under current climate conditions with respect to a state-of-the-art



158 reanalysis is presented in Section 3. The results of the PGW experiments are given in Section 4.
159 Additionally, we will analyze the possible future changes of the medicane. A more insightful
160 discussion on the competing roles of a warmer atmosphere and ocean in the medicane, respectively,
161 will be examined in Section 5. Finally, the concluding remarks of this study will be provided in
162 Section 6.

163

164 **2. Data, Model, and Methodology**

165 In this study, ERA5 reanalysis data (Copernicus Climate Change Service, 2017) is used to
166 benchmark the medicane Rolf simulation. ERA5 is a state-of-the-art reanalysis system with a high
167 spatio-temporal resolution ($0.25^\circ \times 0.25^\circ$ and 1 hourly). The trajectory of Rolf computed from ERA5
168 data is regarded as the best medicane track in this study. Additionally, we use observational data of
169 the cyclone track produced by the US National Oceanic and Atmospheric Administration (NOAA).
170 This data is available only from 12UTC, 7 to 12UTC, 9 of November in 2011
171 (<https://www.ssd.noaa.gov/PS/TROP/DATA/2011/tdata/med/01M.html>).

172

173 *2.1 WRF Simulation of Rolf under present climate*

174 Simulations of Rolf are performed with the Weather Research and Forecasting (WRF,
175 Skamarock et al., 2008) model version 3.9.1. The experimental domains consist of two nested
176 domains as shown in Fig.1: the first domain has a 15km mesh covering (-14.3386°E , 34.3386°E)
177 and (30.3248°N , 52.6961°N) and the second one has a 5km mesh covering (-3.9688°E , 12.4400°E)
178 and (35.3447°N , 47.5810°N) with 52 vertical layers, respectively. In both domains, a cumulus
179 convection scheme is switched on. Previous studies (e.g., Migliette et al., 2015; Ricchi et al., 2017;
180 Mooney et al., 2018) have shown that simulated medicanes and tropical cyclones are highly
181 sensitive to different combinations of physical schemes. Therefore, we investigated different
182 plausible combinations of physical schemes for Rolf in a 10km-mesh forced by ERA-Interim (Dee
183 et al., 2011) reanalysis data ($0.75^\circ \times 0.75^\circ$, 6 hourly). In this assessment, we used 27 combinations of
184 physical schemes among cumulus convection (Kain-Fritsch (Kain 2004), Betts-Miller-Janjic
185 (Janjic, 1994), Tiedtke (Tiedtke, 1989; Zhang et al., 2011)), microphysics (WSM5 (Hong et al.,
186 2004), WSM6 (Hong and Lim, 2006), Thompson (Thompson et al., 2008)) and planetary boundary
187 layer (Yonsei Univeristy (Hong et al., 2006), Mellor-Yamada-Janjic (Janjic, 1994), Mellor-
188 Yamada-Nakanishi-Niino (MYNN; Nakaish and Niino, 2006; Nakanishi and Niino, 2009; Olson et
189 al., 2019)). The assessment simulations showed that most simulations of Rolf with Tiedtke
190 convection scheme make a landfall around southern France successfully and all simulated
191 medicanes with Kain-Fritsch and Betts-Miller-Janjic convection schemes make an incorrect landfall
192 over the Sardinia Island or decay over the Mediterranean Sea without landfall (not shown). Based



193 on the results of this assessment, we select one of the best combinations: Tiedtke, Thompson,
194 MYNN. These three physical schemes are combined with the longwave and shortwave radiative
195 schemes of the Rapid Radiative Transfer Model (Mlawer et al., 1997) and NOAA 4-layer land
196 surface model (Chen and Dudhia, 2001a, b). Initialization and lateral boundary conditions are taken
197 from ERA-Interim 6-hourly reanalysis data ($0.75^\circ \times 0.75^\circ$). The lower boundary condition of sea
198 surface temperature (SST) is obtained from daily OISST data with $0.25^\circ \times 0.25^\circ$ horizontal
199 resolution. The simulations are integrated from 0000UTC on 05-Nov-2011 to 2300UTC on 10-Nov-
200 2011. These simulations are referred to PRS hereafter. ERA-Interim is selected as the driving data
201 for our WRF simulations to maintain consistency between the spatial resolutions of the PGW delta
202 calculated from the CMIP5 ensemble and the reanalysis data used for the initial and boundary
203 conditions (in particular for atmospheric variables). We also investigated the representation of the
204 medicane Rolf in ERA-Interim and found a cyclone track similar to ERA5 (see Section 3 for
205 details).

206

207 *2.2 WRF simulation of Rolf under warmer climate*

208 To investigate how future global climate change influences the medicane, a pseudo global
209 warming (PGW, e.g., Parker et al., 2018; Mooney et al., in review) experiment is employed. In the
210 PGW framework, boundary conditions of WRF are perturbed by the monthly-mean values of global
211 climate change (Δ). This is estimated by simulations of climate projections from CGCMs. In other
212 words, we can simulate the medicane Rolf under a virtually warmed climate. In this study, we
213 obtain the PGW Δ from the ensemble mean (see Table 1) of 19 simulations used in the Coupled
214 Model Inter-comparison Project 5 (CMIP5, Taylor et al., 2012) between 2036-2065 and 1976-2005.
215 The PGW Δ contains perturbed values for zonal and meridional winds, temperature, relative
216 humidity, geo-potential, SLP, SST, and skin temperature. The new boundary conditions including
217 the global warming can be expressed as,

218

$$219 \quad BC_{PGW} = BC_{PRS} + \Delta, \text{ where}$$

$$220 \quad \Delta = CMIP5_{2036-2065} - CMIP5_{2005-1976} \quad (1),$$

221 here, BC represents any of the variables used as boundary conditions for WRF.

222 In the PGW experiment, we perform three different simulations: (1) PGW Δ is added to all
223 the values of boundary conditions (PGW_{ALL}), (2) added only to SST and skin temperature
224 (PGW_{SST}), and (3) added only to the atmospheric variables (PGW_{ATMS}). This enables an
225 investigation of the relative roles of projected future changes in the atmosphere and ocean in the
226 development and modification of the medicane. Other experimental configurations of PGWs are the



227 same as those in PRS (see section 2.1). Figure 2 provides the PGW Δ for SSTs and a vertical profile
228 of atmospheric temperature and relative humidity (averaged over the 5km-mesh domain in Fig. 1)
229 for the PGW experiments in this study. In the Mediterranean Sea, the SST increases approximately
230 2°C in Fig. 2b (also shown by Somot et al., 2006). The troposphere is entirely warming by 2 to 3°C
231 in Fig. 2c. In contrast, projections of the relative humidity in the troposphere tend to be reduced
232 under global warming. These projected thermodynamical responses to global warming can lead the
233 Mediterranean climate to be warmer and drier (e.g., Giorgi and Lionello, 2008). To our knowledge,
234 the present study is the first investigation to employ the PGW method to a tropical-like cyclone in
235 the Mediterranean Sea.

236

237 2.3 Estimation of cyclone phase

238

239 For a trajectory of observed and simulated medicanes, the minimum SLP is tracked from
240 00UTC-06-Nov-2011 until 12UTC-09-Nov-2011. If the medicane makes a landfall before 12UTC-
241 09-Nov-2011, the tracking is ceased. One remarkable characteristic of medicanes is the cyclonic
242 system transitions from extratropical to tropical (e.g., Gaertner et al., 2018). Hart (2003) proposes
243 an objective measurement of cyclone phase space defined as,

244

$$245 \quad \left. \frac{\partial(\Delta Z)}{\partial \ln p} \right|_{900 \text{ hPa}}^{600 \text{ hPa}} = -|V_T^L| \quad (2) \quad \text{and} \quad \left. \frac{\partial(\Delta Z)}{\partial \ln p} \right|_{600 \text{ hPa}}^{300 \text{ hPa}} = -|V_T^U| \quad (3)$$

246 where,

$$247 \quad \Delta Z = Z_{\max} - Z_{\min} \quad (4).$$

248 Z_{\max} and Z_{\min} denote the maximum and minimum geopotential height at a pressure level
249 within 2.5° (for ERA5) and 250km (for WRF simulations) radius around the medicane centre. The
250 upper- and lower- tropospheric thermal wind relation is estimated by equations (2) and (3),
251 respectively. As shown by Hart (2003), in the extratropical phase, the cyclone has deep cold core
252 and the values of (2) and (3) are negative. In addition, the tropical cyclone has a deep warm core
253 with positive values for (2) and (3). In this study, the thermal wind relation is estimated every 50
254 hPa from 900 to 300 hPa and the cyclone phase indices of (2) and (3) are defined as mean of the
255 values every 50hPa between 600 and 300 hPa and between 600 and 900 hPa.

256

257 3. Simulation of Medicane Rolf under present climate

258 In this section we examine the results of PRS to assess ability of our WRF setup to simulate
259 Rolf. Figure 3a gives a best track of Rolf estimated by ERA5. The best track is based on the



260 minimum value of SLP every 3 hour. At the beginning (0000UTC, 6-Nov), the cyclone centre was
261 identified around 5°E and 42°N in the Mediterranean Sea. This location of the cyclone centre is
262 associated with a cut-off low originated from the north Atlantic Ocean (not shown). The cyclone
263 moves southward and crosses the Balearic Islands from 1200UTC, 06-Nov to 0000UTC, 07-Nov.
264 Afterward, the cyclone shifts its direction to the east and north. According to previous studies (e.g.,
265 Dafis et al., 2018), Rolf reaches its peaks of deep cumulus convection from 0000 to 0300UTC on
266 08-Nov over the Mediterranean Sea. At 0000UTC on 09-Nov, Rolf approaches southern France and
267 part of it makes a landfall. After landfall, Rolf's intensity decays as it shifts northwestward and
268 disappears. The cyclone track of ERA5 is in good agreement with the NOAA observations. Even
269 though the location of Rolf after 0000UTC on 09-Nov is somewhat different, ERA5 observes the
270 westward progression of Rolf after 0000UTC on 09-Nov. The cyclone track of PRS is given in Fig.
271 3b. In general, the PRS simulation reproduces the observed cyclone track from the beginning to the
272 end of its life cycle. While the cyclone passes slightly more north of the Balearic Islands (landfall
273 over Ibiza), the cyclone moves northward at 0000UTC on 07-Nov and approaches southern France
274 at 00-09-Nov. In ERA5, Rolf shifts westward after the partial landfall on southern France, but the
275 PRS-simulated Rolf progresses northward and makes a complete landfall over southern France and
276 disappears afterward.

277 The phase shift of the cyclone of ERA5 and PRS is shown in Figure 4 as cyclone phase
278 space defined by Hart (2003) (see the details of definition in section 2.3). In ERA5, the cyclone has
279 a deep cold core at 0000UTC on 06-Nov (Figs. 4a and 4b), which is one of the characteristics of
280 extratropical cyclones. As time elapses, the cyclone transitions from a deep cold core to a shallow
281 warm core. In particular, the upper troposphere loses the feature of cold core during 7 of November
282 (Fig. 4a). After 1200UTC on 07-Nov, the warm core develops more vertically and consequently the
283 cyclone has a deep warm core structure at 0000UTC on 08-Nov. Approaching southern France at
284 2100UTC on 08-Nov (Fig. 3a), the upper troposphere shifts to a weak cold core indicating the
285 decay of the tropical-like cyclone. In PRS, at the beginning, the cyclone already develops with a
286 shallow warm core even though the upper troposphere has a strong cold core (Figs. 4c and d). This
287 structure of shallow warm core continues until 12-06-Nov and the cyclone forms a deep warm core
288 at 00-07-Nov (Fig. 4c and 4d), which is earlier than ERA5 (Figs. 4a and b). However, there is a still
289 cold core at 300 hPa (Figs. 4c) and at 00-08-Nov the simulated cyclone forms a completely deep
290 structure with strong warm core in the lower troposphere (Figs. 4c and d). This timing is almost
291 consistent with ERA5 even though the warm core is stronger in PRS than in ERA5 (Figs. 4b and
292 4d). Equally, the upper troposphere shifts again to cold core around 2000UTC on 08-Nov when
293 Rolf made a landfall partially over southern France (Fig. 3b).



294 Along this cyclone track, a time sequence of SLP of the cyclone centre is given in Fig. 5a. In
295 ERA5, the SLP drops down to 996 hPa at 03-06-Nov when the cyclone still has a deep cold core
296 (Fig. 4a). After this peak, the SLP keeps increasing to 1006 hPa until 0900UTC on 07-Nov and
297 again the SLP centre shrinks down to 1002 hPa at 0300UTC on 08-Nov when Rolf has a peak of
298 deep convection (e.g., Dafis et al., 2018) and a deep warm core is structured through the entire
299 troposphere (Figs. 4a and b). In the simulated Rolf, the SLP also drops down to 991 hPa at
300 0600UTC on 06-Nov during the preconditioning period of the tropical-like cyclone. Similar to
301 ERA5, the SLP of the cyclone increases to 996 hPa until 0000UTC on 07-Nov, decreases again, and
302 consequently the deepening of the low pressure reaches 990 hPa between 0000 and 0300UTC on
303 08-Nov (Fig. 5a). After this peak, the SLP of the simulated cyclone increases rapidly approaching
304 southern France (the depression is weakened to 1002 hPa after 20-08-Nov). The development of the
305 cyclone can be partially linked with the water vapour gained by the cyclone as shown in Fig. 5b. In
306 ERA5, the latent heat flux gradually increases from the beginning until 0000UTC on 07-Nov (from
307 100 to 220 Wm^{-2}). After 0600UTC on 07-Nov, the latent heat flux gradually decreases and slightly
308 increases until 03-08-Nov when the SLP depression is maximum. The latent heat flux decreases
309 gradually again following the approach to the partial landfall over southern France. In PRS as well,
310 the latent heat flux gained by the cyclone increases from the beginning until 06-07-Nov (from 140
311 to 320 Wm^{-2}) even though this is stronger than in ERA5. After this peak, the latent heat flux begins
312 to reduce and is slightly enhanced at 00-08-Nov. Similar to ERA5, the latent heat flux drops again
313 until the landfall over southern France. Surface flux and the corresponding diabatic heating is an
314 energy source of transition from extratropical to subtropical and tropical-like cyclones (e.g.,
315 Emanuel, 2005; Qutián-Hernández et al., 2020). Rolf also obtains a huge amount of water vapour
316 from the underlying sea surface during its phase transition and development. The difference in
317 intensity and transition timing between ERA5 and PRS may be caused by the difference in
318 evaporation and condensation the cyclone gains. However, PRS is able to realistically reproduce the
319 medicane Rolf and we will investigate the impact of climate change on Rolf in the next section.

320

321 **4. Simulation of Medicane Rolf under 1.5°C global warming**

322 As explained in Section 2, we explore how Rolf is affected by the future climate change
323 (middle of the 21st century), which corresponds to global warming of 1.5°C using the pseudo global
324 warming (PGW: e.g., Schär et al., 1996; Rasmussen et al., 2011; Parker et al., 2018) technique. In
325 addition to the effects of climate change, the relative roles of the atmosphere and the ocean in the
326 modulations of medicane Rolf are also investigated separately in this section.

327 Figure 6 shows the simulated cyclone tracks of Rolf in the PGW experiments. PGW_{ALL}
328 reproduces quite a similar cyclone track to that in PRS (Figs. 6a). From the beginning to 0000UTC



329 on 07-Nov, the cyclone moves southward approaching the Balearic Islands. After 0000UTC on 07-
330 Nov, the cyclone progresses northward and makes landfall at 2100UTC 08-Nov. While this
331 behaviour is not considerably different from that in PRS, a few other differences can be detected.
332 Under the future climate change, Rolf does not make landfall over Ibiza and the latitude where the
333 cyclone shifts its direction from south to north is relatively higher than that in PRS (Fig. 6a). The
334 cyclone track shifts more westward approaching southern France (4°E in PGW_{ALL} and 6°E in PRS)
335 and the cyclone makes landfall slightly earlier than PRS. These modifications in the cyclone track
336 are more remarkable in PGW_{SST} shown in Fig. 6b. The simulated medicane changes its marching
337 direction to the north at much higher latitude (higher than 40°N), far from the Balearic Islands, at
338 0000UTC on 07-Nov. After this shift, the cyclone moves northward similar to PRS and PGW_{ALL},
339 but the timing of direction change is earlier by 6 hours and its direction shifts more westward than
340 PRS and PGW_{ALL} (Rolf in PGW_{ALL} begins to move westward after 0000UTC on 08-Nov in Fig.
341 6a). Due to those modifications, the simulated medicane achieves landfall over southern France at
342 3.8°E (slightly more western than PGW_{ALL}) and the landfall is much earlier than PRS and PGW_{ALL},
343 which is at 1200UTC on 08-Nov. Interestingly the PGW_{ATMS} simulation of Rolf shows a clearly
344 opposite tendency of changes to PGW_{ALL} and PGW_{SST} in Fig. 6c. The simulated cyclone strikes
345 Ibiza like PRS, but the cyclone in PGW_{ATMS} progresses more southward while the cyclone in PRS
346 moves eastward after this landfall on Ibiza (Figs. 6c). The cyclone in PGW_{ATMS} still moves
347 eastward after 0000UTC on 07-Nov and finally changes its direction to north at 1200UTC on 07-
348 Nov, which is later by 6 and 12 hours than PRS or PGW_{ALL} and PGW_{SST}. Instead of moving
349 westward, the cyclone in PGW_{ATMS} orientates to the northeast at 0000UTC on 08-Nov and
350 approaches south France around 7°E at 0000UTC on 09-Nov shown in Fig. 6c. The response of the
351 cyclone track to climate change seems different between PGW_{ALL}/PGW_{SST} and PGW_{ATMS} and we
352 see how the other features of the cyclone will change in the PGW experiments.

353 Figure 7a gives a time series of SLP in the cyclone centre of PGWs along the cyclone tracks
354 in Figs. 6. Rolf in PGW_{ALL} develops the SLP centre in quite a similar way to Rolf in PRS. In the
355 beginning, the SLP depresses once to 991 hPa at 0700UTC on 06-Nov and increases the SLP of the
356 centre until 0000UTC on 07-Nov. Again, the SLP reduces and reaches the other minimum of
357 990hPa at 0000 to 0300UTC on 08-Nov. While the SLP of the cyclone centre is almost identical
358 between PRS and PGW_{ALL}, the strength of deepening is different. Figure S1 shows the scalar of
359 SLP gradient for PRS and PGW_{ALL} at 0000UTC on 08-Nov. It is obvious that the SLP gradient is
360 much stronger in the PGW_{ALL} than in the PRS around the peak time indicating that the warmer
361 climate tends to deepen the centre of the medicane, which could be linked to the changes in wind
362 and precipitation (described later). Such a modest enhancement of the medicane has been concluded
363 by Cavicchia et al. (2014) by climate projection experiments. Compared to PRS, the cyclone in



364 PGW_{ALL} decays relatively rapidly after the peak at 0300UTC on 08-Nov, in particular, after
365 1200UTC on 08-Nov. This is likely to be due to the earlier time of landfall of the PGW_{ALL} cyclone
366 over southern France (Figs. 3b and Fig.6a). Inversely, the SLP of the PGW_{SST} cyclone drops down
367 intensively to 985 hPa from the beginning to 0700UTC on 06-Nov. The SLP centre in the PGW_{SST}
368 does not increase and continues to reduce the SLP until 1900UTC on 07-Nov to 963 hPa, which is
369 the earlier peak time and much stronger depression of the cyclone centre than those in PRS and
370 PGW_{ALL}. After this peak, the cyclone in the PGW_{SST} decays quite rapidly (approximately 20 hPa
371 per 12 hours between 0000UTC and 1200UTC on 08-Nov) associated with the earlier landfall time
372 than PRS and PGW_{ALL} (Figs. 3b, 6a and 6b). After the landfall, the cyclone continues to decay
373 further and almost disappears at 2300UTC on 08-Nov over southern France. It is of interest that in
374 PGW_{ATMS} the depression of SLP is substantially reduced throughout cyclone tracking. While In the
375 beginning, the SLP of the cyclone centre is almost identical with those of PRS and PGW_{ALL}, the re-
376 depressing of the cyclone centre after 0000UTC on 07-Nov is much weaker than PRS and PGW_{ALL}.
377 The second peak of low SLP is detected at 2300UTC on 07-Nov (slightly earlier than PRS and
378 PGW_{ALL}), but it shrinks only to 1000 hPa. The cyclone begins to decay gradually after the second
379 peak. Interestingly, this result suggests that the role of future climate change in the atmosphere and
380 ocean have competing effects on the medicane development.

381 Figure 7b gives a time series of latent heat flux gained (averaged) by the simulated cyclone
382 within a radius of 250 km. The evaporation in PGW_{ALL} is relatively larger than that in PRS, in
383 particular, from the beginning to 1200UTC on 07-Nov (approximately 50 W/m² higher at largest).
384 The temporal variation in evaporation along the cyclone track is almost identical between PRS and
385 PGW_{ALL}. Correspondingly to the more rapid decay of the cyclone in PGW_{ALL}, the latent heat flux
386 in PGW_{ALL} decreases more rapidly than PRS after 0000UTC on 08-Nov. In PGW_{SST}, the simulated
387 cyclone obtains much more water vapour from the underlying warmer SST. From the beginning,
388 the latent heat flux is about double that in PRS and increases up to 500 W/m² until 1200UTC on 07-
389 Nov continuing to 0000UTC on 08-Nov with the same amplitude. The uptake of water vapour
390 drops suddenly after 0000UTC on 08-Nov and becomes lesser than that in PRS at 0600UTC on 08-
391 Nov and is diminished to almost zero after the earlier landfall. Inversely, the evaporation in
392 PGW_{ATMS} is inactivated compared to that in PRS during the entire period of cyclone tracking (100
393 W/m² at smallest). However, the temporal variation in evaporation is quite similar to that in PRS
394 having a peak around 06-07-Nov. The decreasing rate of the evaporation after the peak in PGW_{ATMS}
395 is relatively more moderate than those in PGW_{ALL} and PGW_{SST} due to the later time of the landfall
396 (Fig. 6c). While the uptake of water vapour differs among PGWs, its peak leads the maximum of
397 the medicane similarly by 6 to 12 hours (Figs. 7a and 7b).



398 In PRS, the precipitation associated with the cyclone is intense at 0000UTC on 06-Nov and
399 decreases until 1200UTC on 06-Nov in Fig. 7c. That could be associated with deep cumulus
400 convection due to the initial cut-off low and trigger of warm seclusion (e.g., Mazza et al., 2017; Fita
401 and Flaounas, 2018). After 1200UTC on 06-Nov, the precipitation remains in a relatively small
402 with some fluctuations before increasing again at 1200UTC on 07-Nov reaching a peak around
403 2100UTC on 07-Nov, which is somewhat earlier than the peak of SLP depression (Fig. 7a).
404 Coinciding with the reduction in the SLP depression, the precipitation decreases again after the
405 peak. The precipitation in PGW_{ALL} shows quite a similar variation to that in PRS until 1200UTC on
406 07-Nov although the precipitation is slightly stronger. While the precipitation in PGW_{ALL} is
407 reactivated at the same time as PRS, its amplitude of the peak around 21-07-Nov is much larger
408 than that in PRS. That is, the simulated cyclone in PGW_{ALL} can obtain more energy from diabatic
409 heating than PRS resulting in a stronger deepening of SLP shown in Fig. S1. This stronger
410 precipitation can be associated with an enhanced uptake of the water vapour in PGW_{ALL} as shown in
411 Fig. 7b. In PGW_{SST}, the precipitation until 1000UTC on 06-Nov varies quite similarly to that in
412 PRS and PGW_{ALL}, however the precipitation keeps its relatively strong intensity and consequently,
413 the difference from PGW_{ALL} and PRS is large during the cyclone track. After 0000UTC on 07-Nov,
414 precipitation gets more activated and its peak reaches 2.7 mm/hour before 0000UTC on 08-Nov.
415 Similar to PGW_{ALL}, after the peak the precipitation is abruptly reduced due to the earlier timing of
416 the landfall (Fig. 6b). This intense rainfall can be associated with the fact that the cyclone is fueled
417 with abundant water vapour in PGW_{SST} (Fig. 7b). The precipitation of PGW_{ATMS} also shows an
418 identical variation with PRS in the beginning of the track. Associated with the moderate latent heat
419 flux in Fig. 7b, the precipitation is less during the whole lifecycle of the cyclone and has a peak at
420 1700UTC on 07-Nov with a smaller amplitude than those in PRS and other PGWs.

421 Figure 7d illustrates a time series of hourly maximum wind speed (MWS, hereafter) around
422 the cyclone in each simulation. The MWS is defined as a value of 10m-wind speed at a grid where
423 the maximum value is detected every hour within 250km radius of the cyclone. In PRS, from
424 0000UTC on 06-Nov until 0000UTC on 07-Nov, the MWS decreases and increases until 0800UTC
425 on 08-Nov. This variation is roughly consistent with that in the SLP (Fig. 7a). However, the MWS
426 has another peak at 1800UTC on 08-Nov. In PGW_{ALL}, the hourly changes in MSW are similar to
427 those in PRS, but that is stronger than in PRS through the most lifecycle (at largest, 6m/s higher in
428 PGW_{ALL}). After 1200UTC on 08-Nov, the MWS in PGW_{ALL} abruptly dropped. This could be
429 caused by the earlier landfall in PGW_{ALL} than PRS (Fig. 6a) and therefore, the second peak of the
430 MWS might be missed in PGW_{ALL}. In PGW_{SST}, the MWS does not decrease, but that is reinforced
431 from the beginning until 2200UTC on 07-Nov. While the MWS exceeds to 40 m/s at 1600UTC on
432 07-Nov and commences to decrease gradually at 0000UTC until 1500UTC on 08-Nov, the MWS



433 falls down rapidly afterward due to the earlier landfall (Fig. 6b). In PGW_{ATMS} , during 06 and 07-
434 Nov, the MWS is slightly stronger than that in PRS (but, weaker than PGW_{ALL}). However, the grid
435 number of high wind speed is much less in PGW_{ATMS} than in PRS (not shown here, but a plot of
436 horizontal structure of surface wind speed will be given in Fig. 9). After 0000UTC on 08-Nov (the
437 deep warm core is well defined), the MWS in PGW_{ATMS} is weaker than that in PRS.

438 Figure 8 illustrates a diagram of the cyclone phase space in PGWs. Whilst the phase shift
439 from a shallow to a deep warm core is almost identical in the PRS and PGW_{ALL} , the warm core of
440 PGW_{ALL} simulated cyclone is relatively stronger around the peak of SLP depression (03-08-Nov in
441 Fig. 7a), particularly, in the lower troposphere. This stronger warm core is consistent with the
442 enhanced deepening of the cyclone shown in Fig. S1 and with the enhanced precipitation in Fig. 7c.
443 From 1500UTC to 2100UTC on 08-Nov, the structure of warm core is diminished in PGW_{ALL} and
444 this is due to the earlier landfall than PRS. The cyclone in PGW_{SST} changes its phase from shallow
445 to deep warm core at 0600UTC on 06-Nov (Fig. 8b), which is much earlier than PRS and PGW_{ALL}
446 (at 1500UTC to 1800UTC on 06-Nov in Figs. 4b and 7a). Once the cyclone shifts to tropical-like
447 features, the structure of the deep warm core is strengthened very rapidly and consequently, the
448 simulated cyclone is matured with a much larger value of phase space than PRS and PGW_{ALL} . In
449 turn, the tropical-like structure shrinks abruptly after its mature state and eventually the cyclone is
450 reduced to one with a cold core at 2100UTC on 08-Nov corresponding to the earlier landfall. The
451 phase shift of the cyclone in PGW_{ATMS} is similar to those in PRS and PGW_{ALL} in Fig. 8c. In
452 contrast, after the cyclone is converted into a tropical-like cyclone from 1200UTC to 1500UTC on
453 06-Nov, the development of a deep warm core stagnates in the period of November 7th. The
454 enhancement of deep warm core can be found after the stagnation. However, the cyclone gets its
455 deep warm core matured in a moderate value of the space. There is no rapid reduction of warm core
456 in PGW_{ATMS} since the cyclone achieves the landfall later than other PGWs Fig. 6c.

457 Under global warming, the development of the medicane is modified with respect to that at
458 present (in particular, a moderate intensification as aforementioned from Figs. 6 to 8). Here, we
459 explore the horizontal structure of the medicane. The wind speed of PRS exceeds to 24 m/s at the
460 peak of SLP depression (based on Fig. 7a) in Fig. 9a. The area of high wind speed spreads widely
461 (more than 100 km radius of the cyclone). In PGW_{ALL} , while the radius of high wind speeds
462 appears to be slightly small, the wind speed is 24 m/s over a large part within the radius of 100km
463 (Fig. 9b) and the maximum values (faster than 26 m/s) is larger than that of PRS. This result is
464 consistent with the stronger deepening of the cyclone centre in PGW_{ALL} as shown in Fig. S1.
465 Regarding the extreme intensification in the SLP depression, the surface wind speed is much
466 stronger in PGW_{SST} than PRS and PGW_{ALL} in Fig. 9c. The wind speed exceeds to 30 m/h
467 everywhere within the radius of 100km (except for the centre) and the area where the wind speed is



468 larger than 20 m/s extends to the radius of 150km. In contrast, wind speeds for the cyclone in
469 PGW_{ATMS} are substantially lower. Its maximum of wind speed is 24 m/s, which is equivalent to that
470 in PRS (as shown Fig. 7d, the hourly MWS in PGW_{ATMS} is slightly larger than that in PRS), but the
471 area of high speed winds is obviously diminished in Fig. 9d and the strong wind speed is limited
472 only in the northern sector around the centre (similar spatial limitation can be seen in hourly MSW
473 in PGW_{ATMS} , not shown). Compared to PRS and other PGWs, the size of the simulated cyclone
474 tends to become smaller in PGW_{ATMS} . These changes in intensity of the cyclone correspond well
475 with those of the cyclone phase space (Fig. 8). It is interesting to note the hurricane-like structure
476 and intensity of the cyclone in PGW_{SST} .

477 Figure 10 illustrates the rainband structure of each simulated cyclone during the
478 precipitation peak given in Fig. 7c. In PRS, the cyclone has a spiral band of precipitation around the
479 centre (Fig. 10a). In particular, the precipitation is active (up to 12 mm/h) in the northern sector of
480 the cyclone and the strong rainfall extends to the northeast direction. There is little rainfall in the
481 centre area, which is cloud-free “eye”; this can be easily detected and it is also a key feature of
482 tropical-like cyclones. As seen in Fig. 7c the precipitation of PGW_{ALL} intensifies during its peak in
483 Fig. 10b. Whereas the spiral band of precipitation is likely to be similar to that in PRS in the
484 northern sector, the northeastward-orientated rainband is enhanced significantly (more than 18
485 mm/h). In addition, the precipitation is also more vigorous than PRS in the southern sector, in
486 particular, around the centre the precipitation is more than 10 mm/h and the spiral rainband of the
487 medicane is also reinforced due to projected global warming. The eye of the medicane is identical
488 to that in PRS. The warmer SST enhances the spiral band more effectively in Fig. 10c as shown in
489 Fig. 7c. The precipitation around the centre exceeds 20 mm/h in the southern sector and the
490 northeastward rainband is elongated with intense rainfall. In the far side of the southern sector, the
491 rainband is more activated compared to PGW_{ALL} . Interestingly, the eye of the medicane becomes
492 larger than that in PRS and PGW_{ALL} and is more clearly organized. This is associated with the
493 much deeper depression of SLP in PGW_{SST} (Fig. 7a). Corresponding to the deactivated precipitation
494 due only to the warmer atmosphere (Fig. 7c), the rainband around the cyclone centre in PGW_{ATMS} is
495 reduced significantly as shown in Fig. 10d. While the maximum rainfall is still more than 10 mm/h
496 near the centre, the rainband almost loses its spiral structure and the area of vigorous rainfall
497 decreases. It seems that the eye of the cyclone still survives, but that forms less clearly than other
498 cases. As shown in Fig. S2, the medicane in PGW_{SST} has much a larger cloud-free eye around the
499 centre than PRS and other PGW experiments (witnessed by outgoing longwave radiation) and this
500 intensified medicane can be classified into a hurricane.

501

502 **5. Discussion on relative role of warmer atmosphere and ocean in medicane development**



503 In the previous section we showed that the warmer climate leads to a moderate medicane
504 intensification in agreement with previous studies (e.g., Cavicchia et al., 2014; Tous et al., 2016;
505 González-Alemán et al., 2019). The results also showed more enhanced precipitation, surface wind
506 speed and a SLP deepening around the medicane. Interestingly though, the warmer atmosphere
507 inhibits the medicane development substantially, while the warmer ocean reinforces the medicane
508 dramatically. In this section, we discuss the factors that underlie the different roles of the
509 atmosphere and the ocean in the response of the medicane development to future warming.

510 Figure 11a gives a time function of convective available potential energy (CAPE) averaged
511 within the 250km radius around the cyclone centre. CAPE in PRS increases from the beginning and
512 reaches its peak around 1000UTC on 07-Nov. This peak occurs earlier than the maximum of
513 precipitation as shown in Fig. 7c. In the remaining time, CAPE decreases corresponding to the
514 decay of the cyclone. PGW_{ALL} has a slightly larger CAPE than PRS in particular before the peak of
515 SLP depression. Because the cyclone in PGW_{ALL} makes an earlier landfall, CAPE also drops more
516 rapidly than PRS. Such a difference is most obvious in PGW_{SST} . CAPE in PGW_{SST} becomes much
517 larger at 0600UTC on 06-Nov and the timing of its peaks is relatively earlier than PRS. After the
518 peak, CAPE decreases much more abruptly than PGW_{ALL} due to the earliest time of landfall.
519 Inversely, increase ratio of CAPE in PGW_{ATMS} is more moderate and decaying of CAPE is also
520 more slowly than PRS. Figures 11b-e give CAPE of each WRF simulation at its maximum in Fig.
521 11a. Between PRS and PGW_{ALL} , the cyclone gains more energy in PGW_{ALL} (Figs. 11b and 11c)
522 resulting in the enhanced precipitation and consequently stronger SLP deepening (Fig. 7). In
523 PGW_{SST} , the medicane is also fueled much energy like PGW_{ALL} and the area of large CAPE spreads
524 more widely around the cyclone centre than PRS and PGW_{ALL} (Fig. 11d). This wider area of high
525 CAPE can be consistent with the larger area of high wind speed (Fig. 9c). Contrastingly, CAPE in
526 PGW_{ATMS} shrinks extensively and its size of high CAPE is much smaller than PRS.

527 CAPE is a physical indicator that serves to estimate to what extent energy can be utilized for
528 cumulus convection. In PGW_{SST} , the cyclone is fueled by increased water vapour mainly due to
529 underlying warmer SST (Figs. 2b and 7b). As such the air mass can be saturated more easily than in
530 PRS when background tropospheric temperature and humidity is identical in the two simulations
531 (here, the temperature/humidity of lateral boundary condition is regarded as background
532 temperature/relative humidity, see Section 2). This situation is favourable to gain more CAPE and
533 therefore, PGW_{SST} has much higher CAPE than PRS (Figs. 11a, 11b and 11d). Since the diabatic
534 heating is a source of energy for cyclone development, more CAPE and precipitation enhance the
535 cyclone and the surface wind also increases. This stronger surface wind, in turn, activates more
536 evaporation from the sea surface (via WISHE feedback) and, consequently, the cyclone can be
537 moistened more effectively. It is noticeable that the medicane in PGW_{SST} consumes CAPE more



538 rapidly than in other PGW experiments, which indicates that the WISHE mechanism works more
539 effectively (also evidenced by much stronger MWS in PGW_{SST}). Consequently, the medicane in
540 PGW_{SST} can have a hurricane-like structure of surface wind speed, rainfall, and OLR (Figs. 9c, 10c,
541 and S2c). Conversely, in PGW_{ATMS}, the background troposphere is warmed and drier through the
542 entire troposphere compared to PRS (Fig. 2c). Even though the ocean forcing is similar in PRS and
543 PGW_{ATMS} (since the SST boundary condition does not differ), the warmer temperature and the
544 lower relative humidity due to global warming (Fig. 2c) is unfavorable for condensation. That is,
545 the warmer and drier atmosphere can inhibit cumulus convection and CAPE is reduced. As a result,
546 the diabatic heating is less effectively generated and the SLP depression and corresponding WISHE
547 feedback are also deactivated in PGW_{ATMS} (the hourly MWS is slightly higher in PGW_{ATMS} than
548 PRS before the peak, but the largest MWS is weaker in PGW_{ATMS} than PRS and the area of high
549 wind speed is very limited in PGW_{ATMS} compared to PRS shown in Figs. 7d, 9a, and 9d). The
550 moderate intensification of the medicane in PGW_{ALL} is a consequent of the competition between
551 enhancement due to the warmer SST and suppression due to the warmer/drier atmosphere.
552 However, we need to consider a role of SST change due to surface wind and evaporation. When
553 evaporation is more effective in PGW_{SST} and less in PGW_{ATMS}, the underlying SST can be cooled
554 down and warmed up. That is, the results shown in this study do not contain all the process of air-
555 sea interaction for the impacts of a warmer climate on the medicane. Therefore, we will need to
556 investigate future changes of the medicane with an atmosphere-ocean coupled model (e.g., Akhtar
557 et al., 2014; Mooney et al., 2016; Ricchi et al., 2019) in the future to increase robustness of our
558 results in this study.

559

560 6. Concluding Remarks

561 In this study we investigated the impacts of future climate change on a tropical-like cyclone
562 (medicane) formed in the Mediterranean Sea in a PGW framework with the WRF regional climate
563 model. The main novelty of this work is the investigation of the relative roles of the atmosphere and
564 ocean, respectively in the medicane's response to projected global warming.

565 Based on the assessment experiments for better combination of three physical
566 parameterizations of WRF (Tiedtke for cumulus convection, Thompson for microphysics, and
567 Mellor-Yamada-Nakanishi-Niino for planetary boundary), we simulated the medicane Rolf under
568 present (PRS) and middle future climate adapting PGW technique (e.g., Parker et al., 2018; Mooney
569 et al., in review). In ERA5, the cyclone gradually shifts its phase from extratropical cyclone (deep
570 cold core) to a shallow warm-core cyclone. This finally transitions into a deep warm-core cyclone
571 around 0000UTC on 8th November. After this peak, the cyclone becomes weaker (the SLP
572 depression is reduced). Compared to the best track of ERA5 reanalysis, PRS of WRF simulates Rolf



573 realistically making a landfall over southern France. While the intensity of Rolf is stronger in PRS
574 than in ERA5 partially because of difference in grid size, the SLP deepening decreases to 990 hPa
575 in PRS, which is consistent well with previous studies (e.g., Miglietta et al., 2013). PRS also
576 represents well the phase transition to a tropical-like cyclone even though its conversion into the
577 tropical-like is achieved earlier in time than ERA5.

578 The PGW experiments revealed obvious changes in medicane structure associated with
579 global warming. First, there is a clear impacts on the cyclone track: in PGW_{ALL} and PGW_{SST} , the
580 medicane tends to march over more northern and western pathway and its timing of landfall
581 becomes earlier than PRS. Conversely, the medicane in PGW_{ATMS} shifts more southward and
582 eastward. This difference in cyclone track might not be a random response, but seems to be
583 associated with changes in the intensity of the medicane. In PGW_{ALL} and PGW_{SST} , the medicane is
584 more enhanced in terms of surface wind and precipitation around the cyclone centre (e.g., Cavicchia
585 et al., 2014; González-Alemán et al., 2019) and the degree of intensification is much stronger in
586 PGW_{SST} and PGW_{ALL} (e.g., the hourly maximum wind speed exceeds to 40 m/s in PGW_{SST} in Fig.
587 7d). The cyclone track of the stronger medicane in PGW_{SST} is more to the north and, consequently,
588 makes an earlier landfall than in PGW_{ALL} . Inversely, the medicane in PGW_{ATMS} reduces its
589 intensity to a large extent and perhaps this simulated cyclone can be categorised into a lower
590 category of medicane (i.e. tropical depression), for example, an unclear eye forming in the centre
591 and the smaller size of region with high wind speed. The northward shift in position of the
592 maximum wind speed associated with the medicane is also detected in a climate projection by Tous
593 et al. (2016). The changes in cyclone track shown in this study might be indicative for the results of
594 Tous et al. (2016). However, since our simulations address only one medicane, we will need to
595 investigate the changes in cyclone track due to global warming in other study cases, so that the
596 implication becomes more robust.

597 Our PGW simulations elucidated the counteracting individual contributions of a warmer
598 atmosphere and a warmer ocean to the development of medicane associated with the global
599 warming. Since the warmer and drier atmosphere inhibits cumulus convection indicated by weaker
600 CAPE, the energy due to diabatic heating is not sufficient. This situation can be ineffective to drive
601 the wind-induced surface heat exchange (hourly maximum wind speed is approximately equivalent
602 between PRS and PGW_{ATMS} , but the area of high wind speed is much smaller in PGW_{ATMS} than in
603 PRS). Consequently, the transition from a cut-off low into a tropical-like cyclone tends to be
604 degraded; this is supported by our analysis of PGW_{ATMS} . Conversely, the warmer ocean surface
605 enriches the medicane with moisture, which allows cumulus convection to develop more
606 effectively. With a more efficient energy gain, the medicane growth is enhanced and WISHE (e.g.,
607 Emanuel, 1986) can be also activated, as indicated by the results of PGW_{SST} . Consolidating these



608 reversal effects of warmer (and drier) atmosphere and ocean (through nonlinear processes), the
609 medicane intensifies to a moderate extent by global warming. While the medicane under global
610 warming shows a modest intensification in terms of wind speed and SLP deepening, precipitation
611 presents radical changes during the peak of intensity. This suggests that medicane could be more
612 hazardous due to global warming as concluded by González-Alemán et al. (2019).

613 In this study we have presented novel findings regarding the relative role of atmosphere and
614 ocean in the modulation of medicane development under global warming. It would be interesting to
615 see if other cases of medicanes show a similar response to the warmer atmosphere and ocean. For a
616 better quantification of changes, the simulation and investigation with a regional coupled model for
617 several cases will be desired in the future.

618

619 **Acknowledgement**

620 This study has been carried out under IBERTROPIC project (grant agreement no. CGL2017-
621 89583-R), funded by the Spanish Ministry of Science, Innovation and Universities, the Spanish
622 State Research Agency and the European Regional Development Fund. Koseki S. is supported by
623 Giner de los Ríos 2018/2019 and 2019/2020, which is a scholarship grant by la Universidad de
624 Alcalá. González-Alemán J.J. has been funded through grants BES_2014-067905 and FJC2018-
625 035821-I by the Spanish State Research Agency. The computational resource comes from the
626 Norwegian High-Performance Computing Program resources (NS9039K).

627

628 **Reference**

- 629 Akhtar, N., Brauch, J., Dobler, A., Béranger, K., and Ahrens, B.: Medicanes in an ocean-
630 atmosphere coupled regional climate model. *Nat. Hazards Earth Syst. Sci.*, **14**, 2189-2201,
631 doi:10.5194/nhess-14-2189-2014, 2014.
- 632 Bakkensen, L. A.: Mediterranean Hurricanes and Associated Damages Estimates.
633 *J. Extreme Events*, **4** (2), <https://doi.org/10.1142/S2345737617500087>, 2017.
- 634 Camargo, S., Sobel, A. H., Barnston, A. G., and Emanuel, K. A.: Tropical cyclone genesis
635 potential index in climate models. *Tellus A*, **59**, 428-443, <https://doi.org/10.1111/j.1600-0870.2007.00238.x>, 2007.
- 637 Caniaux, G., Giordani, H., Redelsperger, J.-L., Guichard, F., Key, E., and Wade, M.:
638 Coupling between the Atlantic cold tongue and the West African monsoon in boreal spring
639 and summer. *J. Geophys. Res. Oceans*, **116**, C04003, doi:10.1029/2010JC006570, 2011.
- 640 Cavicchia, L., von Storch, H., and Gualdi, S.: A long-term climatology of medicanes.
641 *Clim. Dyn.*, **43**, 1183-1195, <https://doi.org/10.1007/s00382-013-1893-7>, 2013.
- 642 Cavicchia, L., von Storch, H., and Gualdi, S.: Mediterranean Tropical-Like Cyclones n



- 643 Present and Future Climate. *J. Climate*, **27**, 7493-7501
644 <https://doi.org/10.1175/JCLI-D-14-00339.1>, 2014.
- 645 Chaboureaud, J. P., Pantillon, F., Lambert, D., Richard, E., and Claud, C.: Tropical transition
646 of a Mediterranean storm by jet crossing. *Q. J. Roy. Meteorol. Soc.*, **138**, 596-611,
647 <https://doi.org/10.1002/qj.960>, 2012.
- 648 Copernicus Climate Change Service : ERA5: First generation of ECMWF atmospheric
649 reanalyses of the global climate. Copernicus Climate Change Service Data Store (CDS),
650 *data of access*. <http://cds.climate.copernicus.eu/cdsapp#!home> , 2017.
- 651 Dafis, S., Rysman, J.-F., Claud, C., and Flaounas, E.: Remote sensing of deep convection
652 within a tropical-like cyclone over the Mediterranean Sea. *Atmos. Sci., Lett.*, **19**, e823,
653 <https://doi.org/10.1002/asl.823>, 2018
- 654 Dee, D. P., Uppala, S. M., Simmons, A. J., Berrisford, P., Poli, P., Kobayashi, S., Andre, U.,
655 Balmaseda, M. A., Balsamo, G., Bauer, P., Bechtold, P., Beljaars, A. C. M., van de Berg, L.,
656 Bidlot, J., Bormann, N., Delsol, C., Dragani, R., Fuentes, M., Geer, A. J., Haimberger, L.,
657 Healy, S. B., Hersbach, H., Hóml, E. V., Isaksen, L., Kåkkberg, P., Köhler, M., Matricardi,
658 M., McNally, A. P., Monge-Sanz, B. M., Morcrette, J.-J., Park, B.-K., Peubey, C., de
659 Rosnay, P., Tavolato, C., Thépaut, J.-N., and Vitart, F.: The ERA-Interim reanalysis:
660 configuration and performance of the data assimilation system. *Q. J. Roy. Meteorol. Soc.*,
661 **137**, 553-597, <https://doi.org/10.1002/qj.828>, 2011.
- 662 Emanuel, K. A.: An air-sea interaction theory for tropical cyclones. Part I: Steady-state
663 maintenance. *J. Atmos. Sci.*, **43**, 585-604, 1986.
- 664 Emanuel, K. A.: Genesis and maintenance of “Mediterranean hurricanes”. *Adv. Geosci.*, **2**,
665 217-220, 2005.
- 666 Fita, L., Romero, R., and Ramis, C.: Intercomparison of intense cyclogenesis events over the
667 Mediterranean basin based on baroclinic and diabatic influence. *Adv. Geoscience*, **7**, 333-342,
668 2006
- 669 Fita, L., and Flaounas, E.: Medicanes as subtropical cyclones: the December 2005 case from
670 the perspective of surface pressure tendency diagnostic and atmospheric water budget.
671 *Q. J. Roy. Meteorol. Soc.*, **144**, 1028-1044, <https://doi.org/10.1002/qj.3273>, 2018.
- 672 Gaertner, M. Á., González-Alemán J. J., Romera R., Domínguez M., Gil, V., Sánchez, E., Gallardo,
673 C., Miglietta, M. M., Walsh, K. J. E., Sein, D. V., Somot, S., Dell’Aquila A., Teichmann,
674 C., Ahrens, B., Buonomo, E., Colette, A., Bastin, S., van Meijgaard, E., and Nikulin, G.:
675 Simulation of medicanes over the Mediterranean Sea in a regional climate model
676 ensemble: impact of ocean-atmosphere coupling and increased resolution.
677 *Clim. Dyn.*, **51** (3) 1041-1057, <https://doi.org/10.1007/s00382-016-3456-1>, 2018.



- 678 Giorgi, F., and Lionello, P.: Climate change projections for the Mediterranean region.
679 *Glob. Planet. Change*, **63** (2-3), 90-104, doi:10.1016/j.gloplacha.2007.09.005, 2008.
- 680 González-Alemán, J. J., Pascale, S., Gutierrez-Fernandez, J., Murakami, H., Gaertner, M. A., and
681 Vecchi, G. A.: Potential Increase in Hazard From Mediterranean Hurricane Activity
682 With Global Warming. *Geophys. Res. Lett.*, **46**, 1754-1764,
683 <https://doi.org/10.1029/2018GL081253>, 2019.
- 684 Hart, R. E.: A Cyclone Phase Space Derived from Thermal Wind and Thermal Asymmetry.
685 *Mon. Wea. Rev.*, **131**, 585-616, 2003.
- 686 Hong, S.-Y., Dudhia, J., and Chen, S.-H.: A revised approach to ice microphysical processes
687 for the bulk parameterization of clouds and precipitation. *Mon. Wea. Rev.*, **132**, 103-120,
688 2004.
- 689 Hong, S.-Y., and Lim, J.-O. J.: The WRF single-moment 6-class microphysics scheme
690 (WSM6). *J. Korean Meteor. Soc.*, **42**, 129-151, 2006.
- 691 Hong, S.-Y., Noh, Y., and Dudhia, J.: A new vertical diffusion package with an explicit
692 treatment of entrainment processes. *Mon. Wea. Rev.*, **134**, 2318-2341.
693 [doi:10.1175/MWR3199.1](https://doi.org/10.1175/MWR3199.1), 2006.
- 694 Janjic, Z. I.: The Step-Mountain Eta Coordinate Model: Further developments of the
695 convection, viscous sublayer, and turbulence closure schemes. *Mon. Wea. Rev.*, **122**,
696 927-945, 1994.
- 697 Jin, F.-F.: Tropical Ocean-Atmosphere Interaction, the Pacific Cold Tongue, and the El Niño-
698 Southern Oscillation. *Science*, **274** (5284), 76-78, doi:10.1126/science.274.5284.76, 1996.
- 699 Kain, J. S.: The Kain-Fritsch convective parameterization: An update. *J. Appl. Meteor.*,
700 **43**, 170-181, 2004.
- 701 Mazza, E., Ulbrich, U., and Klein, R.: The Tropical Transition of the October 1996 Medicane
702 in the Western Mediterranean Sea: A Warm Seclusion Event. *Mon. Wea. Rev.*,
703 **145**, 2575-2595, 2017.
- 704 Miglietta, M. M., Laviola, S., Malvaldi, A., Conte, D., Levizzani, V., and Price, C.: Analysis
705 of tropical-like cyclones over the Mediterranean Sea through a combined modeling and
706 satellite approach. *Geophys. Res. Lett.*, **40**, 2400-2405, doi:10.1002/grl.50432, 2013.
- 707 Miglietta, M. M., Mastrangelo, D., and Conte, D.: Influence of physics parametrization
708 schemes on the simulation of a tropical-like cyclone in the Mediterranean Sea. *Atmos. Res.*,
709 **153**, 360-375, <https://doi.org/10.1016/j.atmosres.2014.09.008>, 2015.
- 710 Miglietta, M. M., and Rotunno, R.: Development mechanisms for Mediterranean tropical-
711 like cyclones (medicanes). *Q. J. Roy. Meteorol. Soc.*, **145**, 1444-1460, doi:10.1002/qj.3503,
712 2019



- 713 Mlawer, E. J., Taubman, S. J., Brown, P. D., Iacono, M. J., and Clough, S. A.:
714 Radiative transfer for inhomogeneous atmospheres: RRTM, a validated correlated- k model
715 for the longwave. *J. Geophys. Res.*, **102**, 16663–16682. [doi:10.1029/97JD00237](https://doi.org/10.1029/97JD00237), 1997.
- 716 Mooney, P. A., Gill, D. O., Mulligan, F. J., and Bruyère, C. L.: Hurricane simulation using
717 different representations of atmosphere-ocean interaction: the case of Irene (2011).
718 *Atmos. Sci. Lett.*, doi:10.1002/asl.673, 2016.
- 719 Mooney, P. A., Mulligan, F. J., Bruyère, C. J., Parker, C. L., and Gill, D. O.: Investigating the
720 performance of coupled WRF-ROMS simulations of Hurricane Irene (2011) in a regional
721 climate modeling framework. *Atmos. Res.*, **215**, 57-74, 2018.
722 <https://doi.org/10.1016/j.atmosres.2018.08.017>.
- 723 Mooney, P. M., Sobolowski, S. P., and Lee, H.: Designing and evaluating regional climate
724 simulations for land use land cover change studies at high latitudes. *Tellus A*, in review,
725 2020.
- 726 Nakanishi, M., and Niino, H.: An improved Mellor–Yamada level 3 model: its numerical
727 stability and application to a regional prediction of advecting fog. *Bound. Layer Meteor.*
728 **119**, 397–407. [doi:10.1007/s10546-005-9030-8](https://doi.org/10.1007/s10546-005-9030-8), 2006
- 729 Nakanishi, M., and Niino, H.: Development of an improved turbulence closure model for the
730 atmospheric boundary layer. *J. Meteor. Soc. Japan*, **87**, 895–912. [doi:10.2151/jmsj.87.895](https://doi.org/10.2151/jmsj.87.895),
731 2009
- 732 Olson, J. B., Kenyon, J. S., Angevine, W. M., Brown, J. M., Pagowski, M., and Sušelj, K.: A
733 Description of the MYNN-EDMF Scheme and the Coupling to Other Components in WRF–
734 ARW. *NOAA Technical Memorandum OAR GSD*, **61**, pp. 37.
735 [doi:10.25923/n9wm-be49](https://doi.org/10.25923/n9wm-be49), 2019.
- 736 Parker, C. L., Bruyère, C. L., Mooney, P. A., and Lynch, A. H.: The response of land-falling
737 tropical cyclone characteristics to projected climate change in northeast Australia. *Clim.*
738 *Dyn.*, **51** (9-10), 3467-3485, <https://doi.org/10.1007/s00382-018-4091-9>, 2018.
- 739 Qutián-Hernández, L., González-Alemán, J. J., Santos-Muñoz, D., Fernández-González, S.,
740 Valero, F., and Martín, M. L.: Subtropical cyclone formation via warm seclusion
741 development: The importance of surface fluxes. *J. Geophys. Res. Atmos.*,
742 <https://doi.org/10.1029/2019JD031526>, 2020.
- 743 Rasmussen, R., Liu, C., Ikeda, K., Gochis, D., Yates, D., Chen, F., Tewari, M., Barlage, M.,
744 Dudhia, J., Yu, W., and Miller, K.: High-Resolution Coupled Climate Runoff
745 Simulations of Seasonal Snowfall over Colorado: A Process Study of Current and Warmer
746 Climate. *J. Climate*, **24** (12), 3015-3048, 2011.
- 747 Ricchi, A., Miglietta, M. M., Barbariol, F., Benetazzo, A., Bergamasco, A., Bonaldo, D., Cassardo,



- 748 C., Falcieri, F. M., Modugno, G., Russo, A., Scavo, M., and Carniel, S.: Sensitivity of
749 a Mediterranean Tropical-Like Cyclone to Different Model Configurations and Coupling
750 Strategies. *Atmosphere*, **8**(5), 92, <https://doi.org/10.3390/atmos8050092>, 2017.
- 751 Ricchi, A., Miglietta, M. M., Bonaldo, D., Cioni, G., Rizza, U., and Carniel, S.: Multi-
752 Physics Ensemble versus Atmosphere-Ocean Coupled Model Simulations for a Tropical-
753 Like Cyclone in the Mediterranean Sea, 2019.
754 *Atmosphere*, **10**(4), 202; <https://doi.org/10.3390/atmos10040202>.
- 755 Schär, C., Frei, C., Lüthi, D., and Davies, H. C.: Surrogate climate-change scenarios for
756 regional climate models. *Geophys. Res. Lett.*, **23**(6), 669-672, 1996.
- 757 Shaltout, M., and Omstedt, A., 2014. Recent sea surface temperature trends and future scenarios for
758 the Mediterranean Sea. *Oceanologia*, **56**, 411-443, <https://doi.org/10.5697/oc.56-3.411>.
- 759 Skamarock, W. C., Klemp, J. B., Dudhia, J., Gill, D. O., Barker, D. M., Duda, M., Huang, X. Y.,
760 Wang, W., and Powers, J. G.: A description of the advanced research WRF version 3. *NCAR*
761 *technical note*, NCAR/TN/u201345?STR, 123pp, 2008.
- 762 Somot, S., Sevault, F., and Déqué, M.: Transient climate change scenario simulation of the
763 Mediterranean Sea for the twenty-first century using a high-resolution ocean circulation
764 model. *Clim. Dyn.*, **27**, 851-879, <https://doi.org/10.1007/s00382-006-0167-z>, 2006.
- 765 Taylor, K. E., Stouffer, R. J., and Meehl, G. A.: An Overview of CMIP5 and the experiment
766 design. *Bull. Amer. Meteor. Soc.*, **93**, 485-498, doi:10.1175/BAMS-D-11-00094.1, 2012.
- 767 Tiedtke, M.: A comprehensive mass flux scheme for cumulus parameterization in large-scale
768 models. *Mon. Wea. Rev.*, **117**, 1779–1800, 1989.
- 769 Thompson, G., Field, P. R., Rasmussen, R. M., and Hall, W. D.: Explicit Forecasts of Winter
770 Precipitation Using an Improved Bulk Microphysics Scheme. Part II: Implementation of a
771 New Snow Parameterization. *Mon. Wea. Rev.*, **136**, 5095–5115.
772 [doi:10.1175/2008MWR2387.1](https://doi.org/10.1175/2008MWR2387.1), 2008.
- 773 Tous, M., Zappa, G., Romero, R., Shaffrey, L., and Vidale, P. L.: Projected changes in
774 medicanes in the HadGEM3 N512 high-resolution global climate model.
775 *Clim. Dyn.*, **47**, 1913-1924, <https://doi.org/10.1007/s00382-015-2941-2>, 2016.
- 776 Zhang, C., Wang, Y., and Hamilton, K.: Improved representation of boundary
777 layer clouds over the southeast pacific in ARW–WRF using a modified Tiedtke cumulus
778 parameterization scheme. *Mon. Wea. Rev.*, **139**, 3489–3513, 2011.
- 779
780
781
782



783 **Figures**

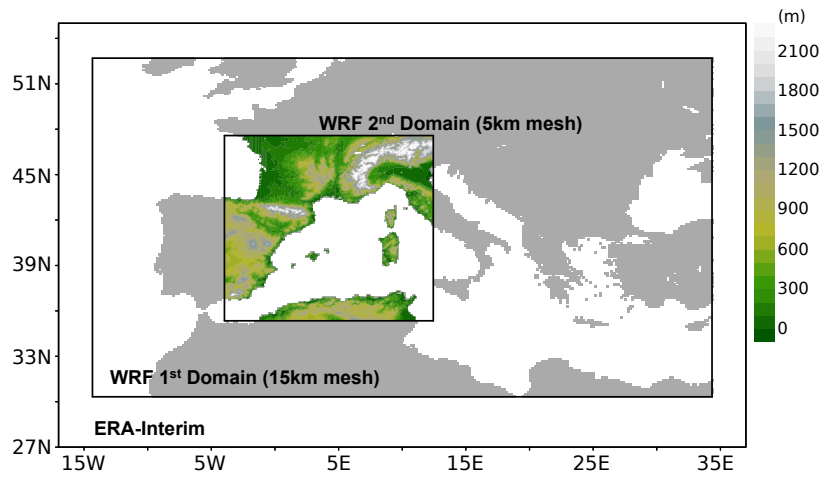


Figure 1. Domains for WRF simulations for medicane, Rolf. Shading in WRF 2nd domain is topography height from MODIS.

784

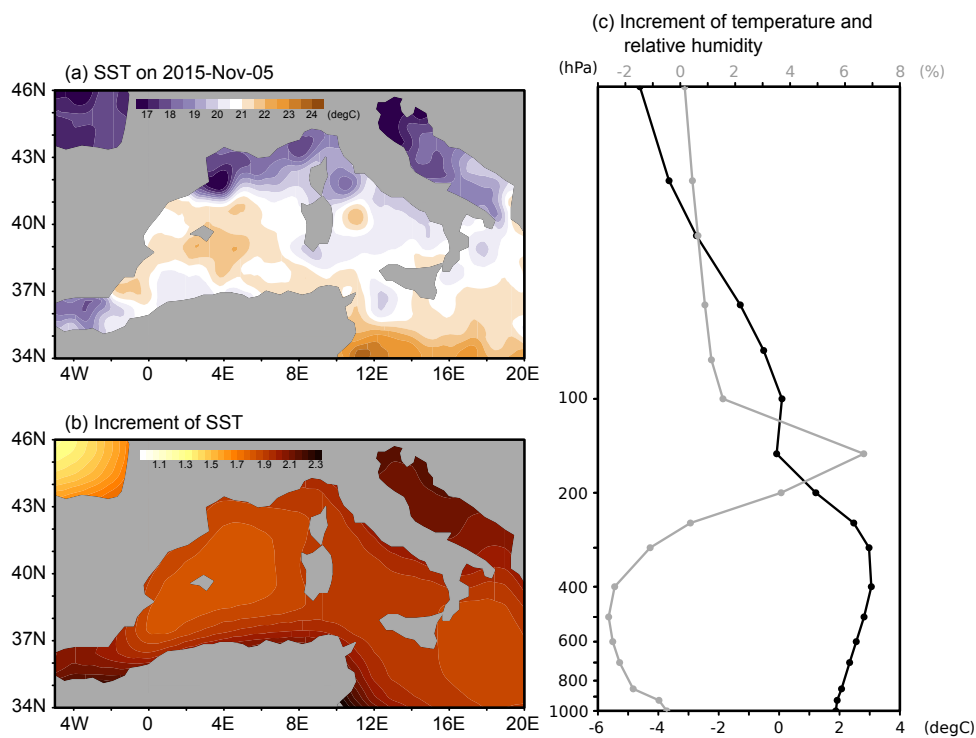


Figure 2.
(a) Sea surface temperature (SST) at 00UTC on 5th November, 2011 in OISST. Increment projected by 18 CMIP5 CGCMs (b) SST and (c) vertical profiles of increment of air temperature and relative humidity averaged over WRF's 2nd domain between 2035-2065 and 1975-2006.

785

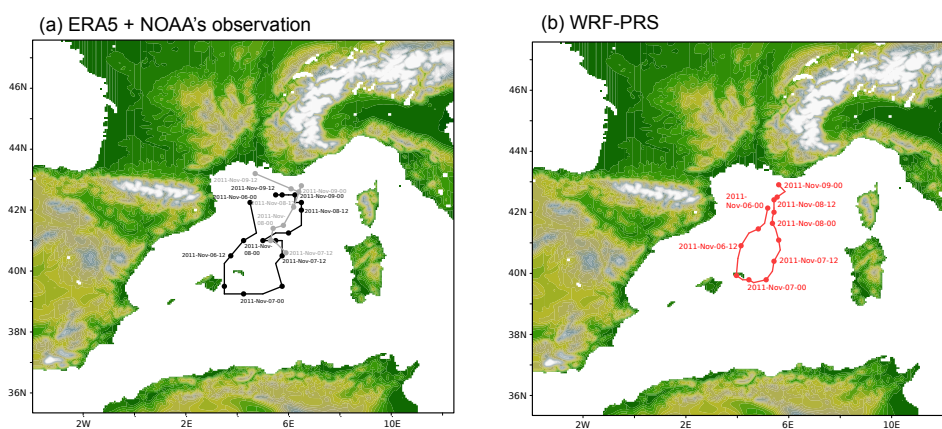


Figure 3.

Trajectory of medicane Rolf by (a) ERA5 (black) and NOAA observation (gray), and (b) PRS, from 00UTC, 6th, Nov, 2011 to 12UTC, 9th, Nov 2011 (for NOAA observation, the trajectory is from 12UTC, 7th, Nov, 2011 to 12UTC, 9th, November, 2011). The tracking is based on the lowest sea level pressure. Note that the track of PRS is until 00UTC, 9th, Nov 2011 because of early landfall on South France.

786

787

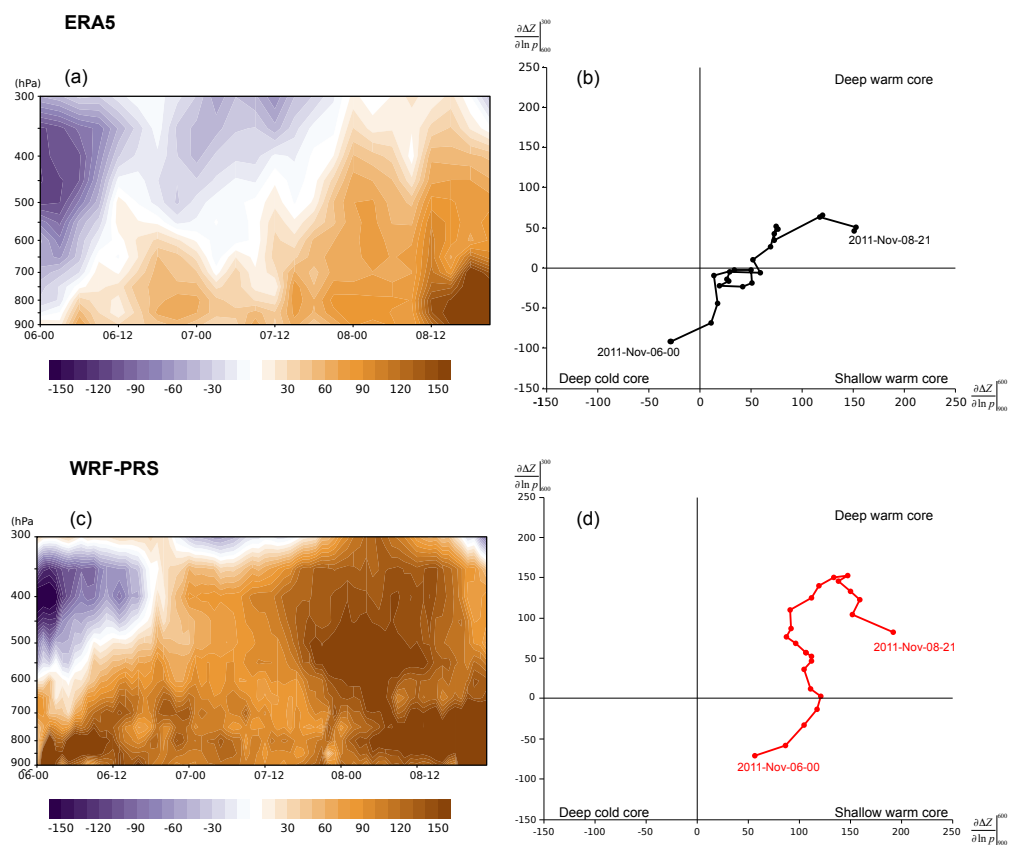


Figure 4. Cyclone phase space defined by Hart 2003. (a) The pressure-time section of cyclone phase space for ERA5. The index is estimated every 50 hPa. (b) The index is projected on upper (600-300 hPa) and lower (900-600 hPa) phase in ERA5. (c) and (d) Same as (a) and (b) except for the WRF PRS simulation.

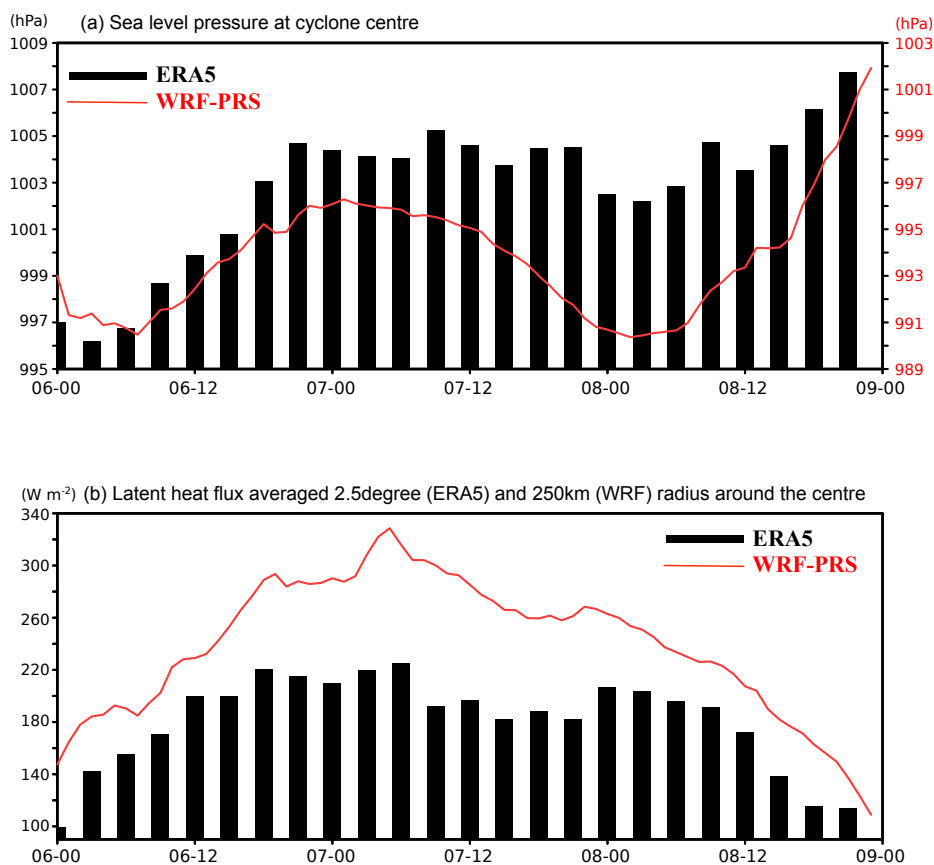


Figure 5. Time series of (a) sea level pressure (SLP) at grid of cyclone centre and (b) latent heat flux averaged within a radius of 2.5 degrees (ERA5) and 250km (WRF-PRS). The black bar and red line denote the variables of ERA5 and WRF-PRS, respectively. Note that the labels in Fig. 5a for ERA5 and PRS are on left and right hand side, respectively.

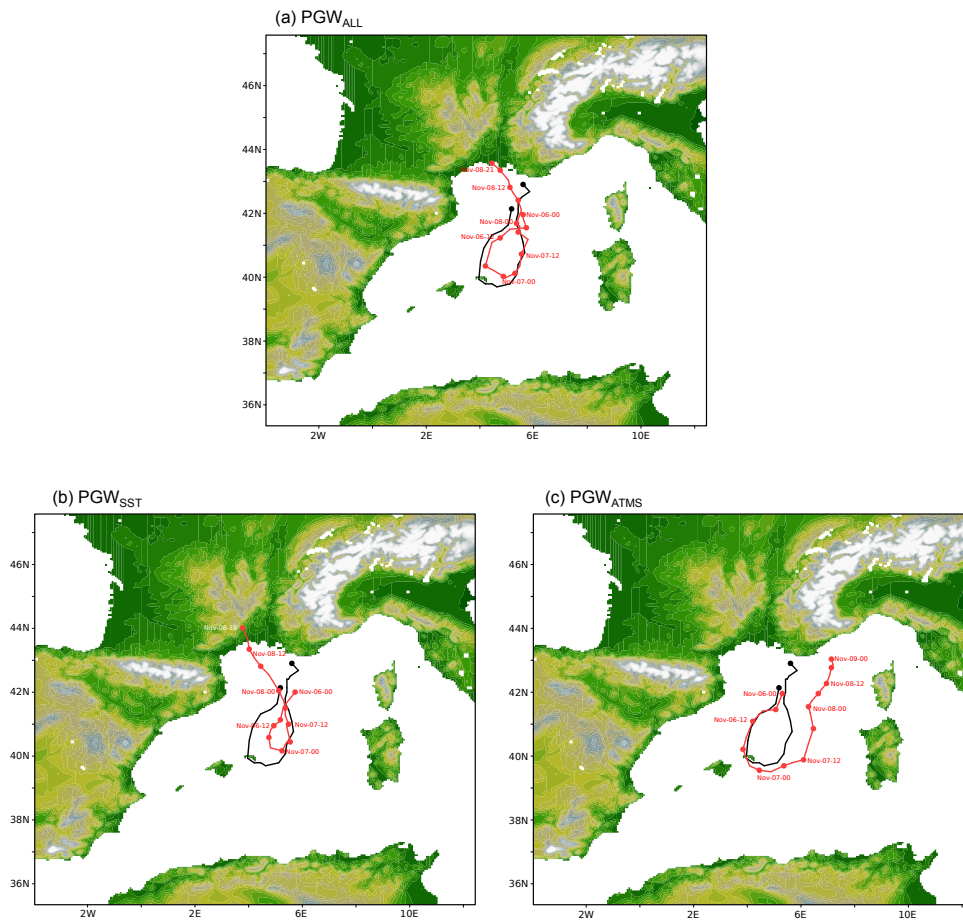


Figure 6.
Same as Fig. 3, but for (a) PGW_{ALL} , (b) PGW_{SST} , and (c) PGW_{ATMS} , respectively.
The black line is the cyclone track for PRS.

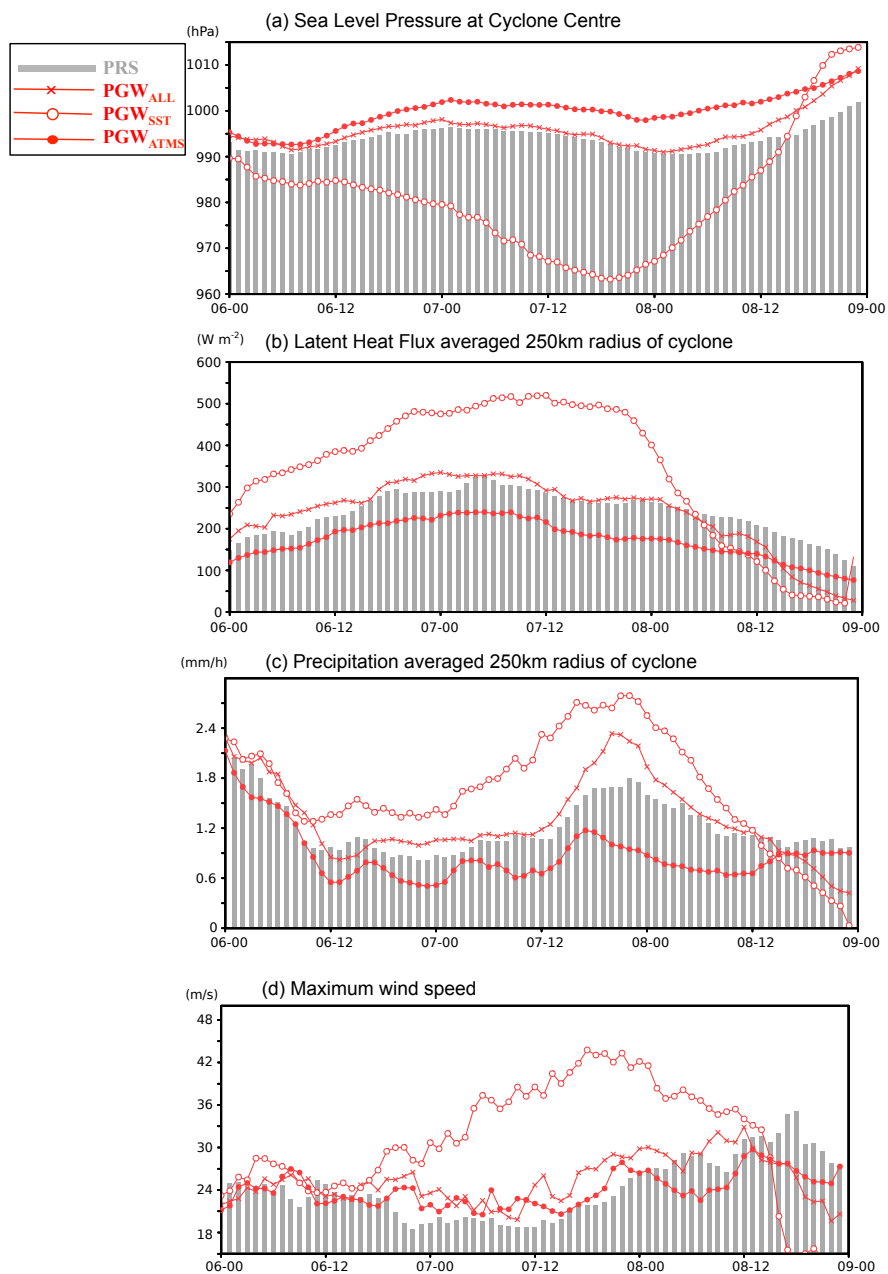


Figure 7. Time series of (a) SLP at grid of cyclone centre, (b) latent heat flux, (c) precipitation averaged, and (d) maximum wind speed within the 250km radius of the simulated medicane. (b) and (c) are averaged value within 250k radius. The gray bar and red lines denote the variables of PRS and PGWs (with different markers), respectively.

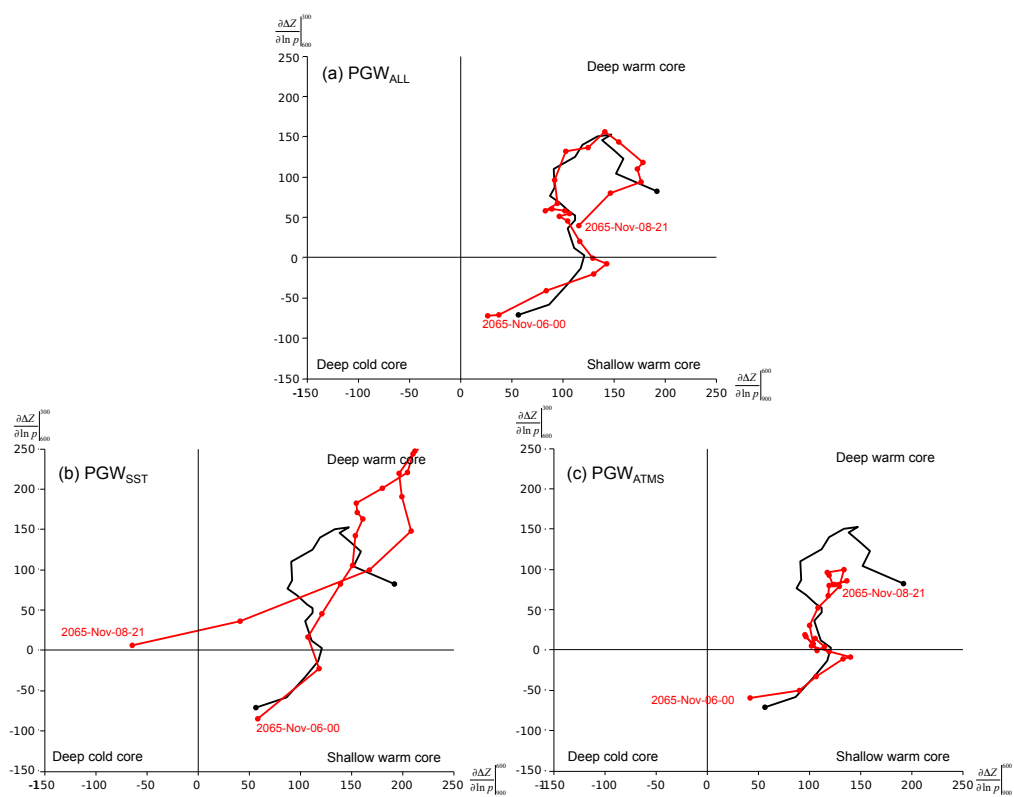


Figure 8. Same as Fig. 4d, but for (a) PGW_{ALL} , (b) PGW_{SST} , and (c) PGW_{ATMS} , respectively. The index of PRS is superimposed by black line.

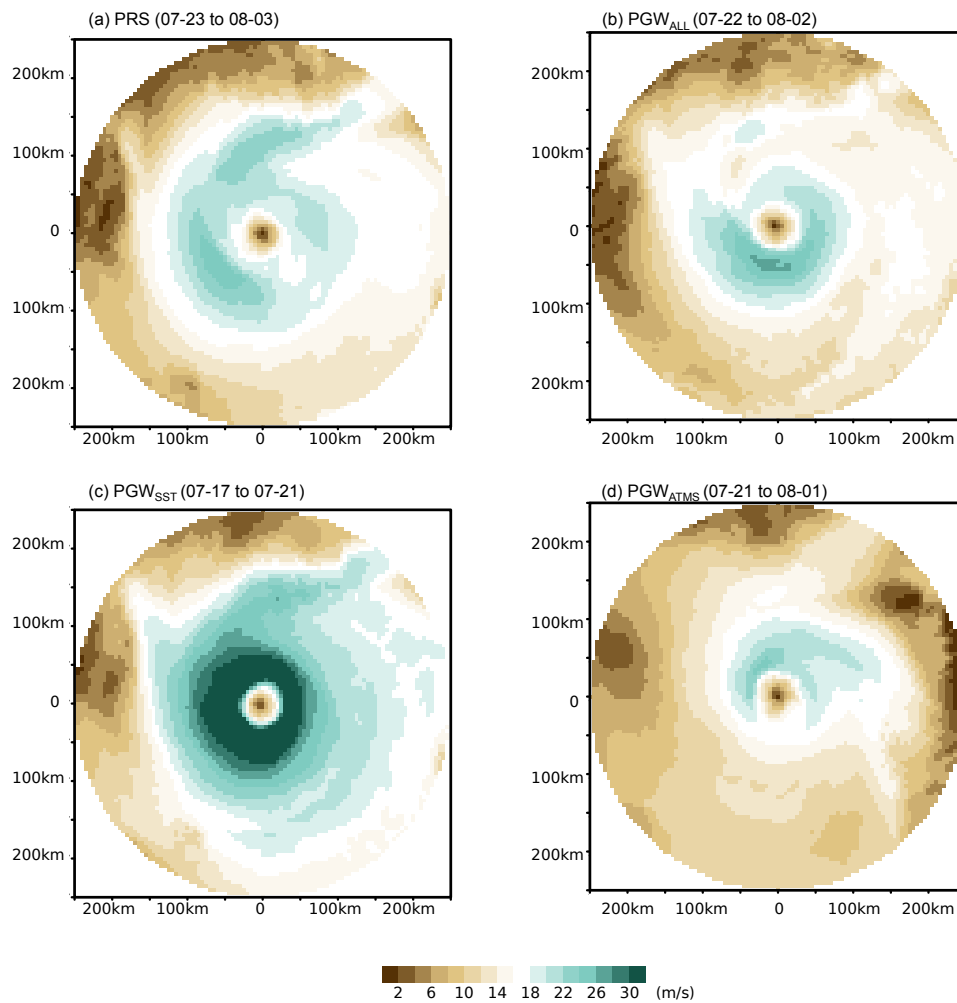


Figure 9. Surface wind speed during SLP minimum (referring to Fig. 7a) for (a) PRS, (b) PGW_{ALL}, (c) PGW_{SST}, and (d) PGW_{ATMS} around the cyclone centre, respectively.

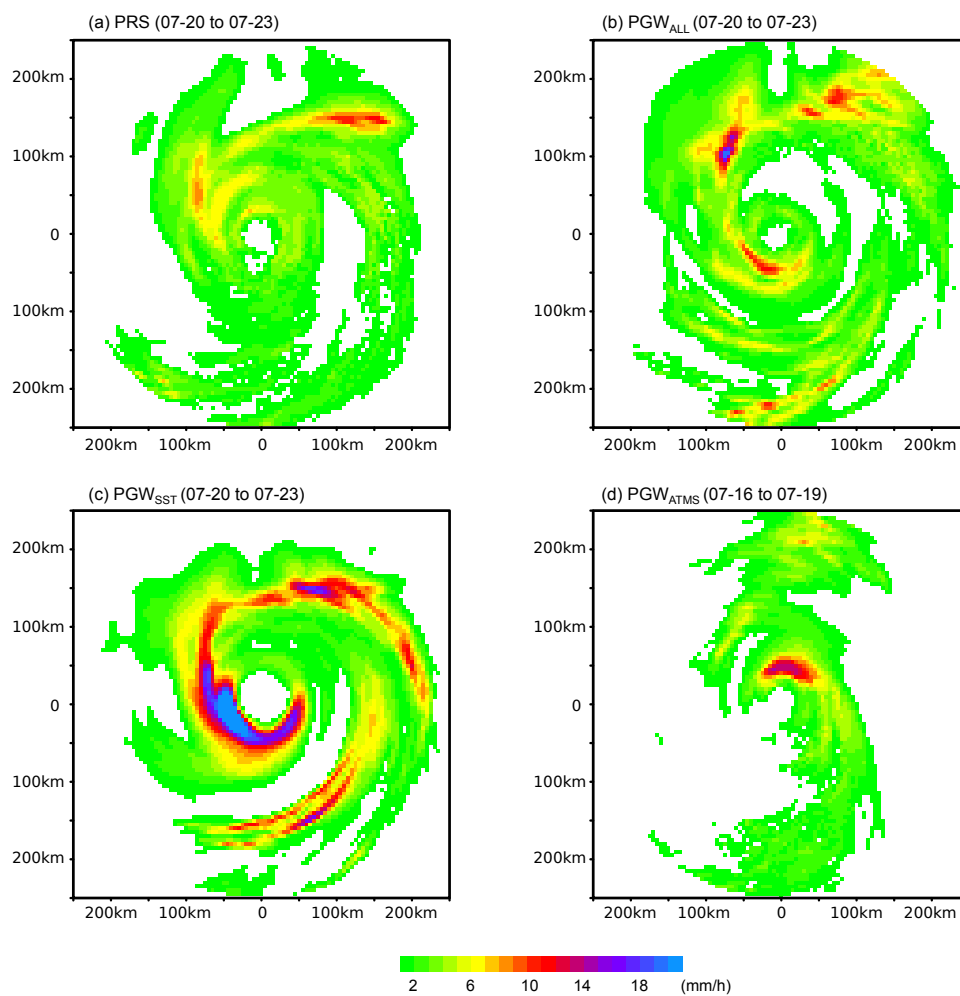


Figure 10. Precipitation during its minimum (referring to Fig. 7c) for (a) PRS, (b) PGW_{ALL}, (c) PGW_{SST}, and (d) PGW_{ATMS} around the cyclone centre, respectively.

794

795

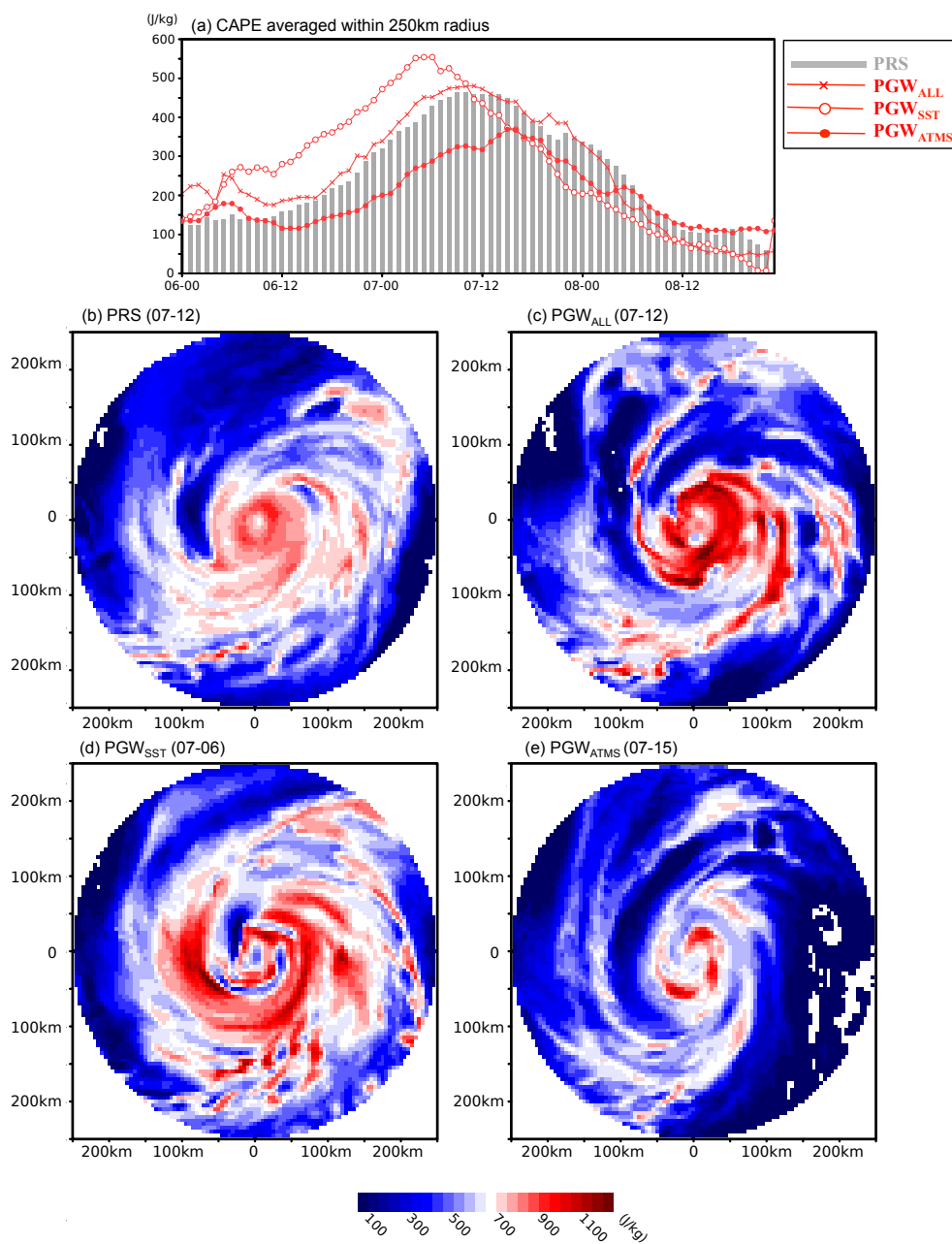


Figure 11. (a) Same as Fig. 7b, but for convective available potential energy (CAPE) and CAPE at its minimum (referring to Fig. 7c) for (b) PRS, (c) PGW_{ALL}, (d) PGW_{SST}, and (e) PGW_{ATMS} around the cyclone centre, respectively.

796
797
798
799
800



801

802 **Table**

Model Name	No. Ensemble Members from Historical Simulation	No. Ensemble Members from RCP8.5 Simulation	Ensemble Members Used	Names of Member Realisations
ACCESS1-3	3	1	1	r1i1p1
CanESM2	5	5	3	r1i1p1, r2i1p1, r3i1p1
CCSM4	6	6	3	r1i1p1, r2i1p1, r6i1p1
CESM1-CAM5	3	3	3	r1i1p1, r2i1p1, r3i1p1
CMCC-CM	1	1	1	r1i1p1
CNRM-CM5	10	5	3	r2i1p1, r4i1p1, r6i1p1
CSIRO-Mk3-6-0	10	10	3	r1i1p1, r2i1p1, r3i1p1
GFDL-CM3	5	1	1	r1i1p1
GFDL-ESM2M	1	1	1	r1i1p1
GISS-E2-H	5	2	2	r1i1p1, r2i1p1
HadGEM2-CC	3	3	3	r1i1p1, r2i1p1, r3i1p1
HadGEM2-ES	4	4	1	r3i1p1

803



INM-CM4	1	1	1	r1i1p1
IPSL-CM5A-MR	3	1	1	r1i1p1
MIROC5	4	3	3	r1i1p1, r2i1p1, r3i1p1
MIROC-ESM	3	1	1	r1i1p1
MPI-ESM-LR	3	3	3	r1i1p1, r2i1p1, r3i1p1
MPI-ESM-MR	3	1	1	r1i1p1
MRI-CGCM3	4	1	1	r1i1p1

Table 1. CMIP5 GCMs used for deriving the climate perturbations for the PGW simulations.